SLAC – PUB – 4318
May 1987
I

# Results from the MAC[1] Vertex Chamber *

HARRY N. NELSON

*Stanford Linear Accelerator Center*
*Stanford University, Stanford, California 94305*

## ABSTRACT

The design, construction, and performance characteristics of a high precision gaseous drift chamber made of thin walled proportional tubes are described. The device achieved an average spatial resolution of 45 $\mu$m in use for physics analysis with the MAC detector. The $B$-lifetime result obtained with this chamber is discussed.

Invited talk presented at *Workshop on Vertex Detectors: State of the Art and Perspectives*, Erice, Italy, September 21-26, 1986.

* This work was supported in part by the Department of Energy under contract numbers DE-AC02-81ER40025 (CU), DE-AC03-76SF00515 (SLAC), and DE-AC02-76ER00881 (UW); by the National Science Foundation under grant numbers NSF-PHY82-15133 (UH), NSF-PHY82-15413 and NSF-PHY82-15414 (NU), and NSF-PHY83-08135 (UU); and by the Istituto Nazionale di Fisica Nucleare.

## INTRODUCTION

In the summer of 1983, the MAC and Mark-II collaborations gave evidence for bottom hadron lifetimes or 1-2 ps[2], based on data accumulated at the PEP $e^+e^-$ storage ring at SLAC. The importance and fundamental nature of this measurement[3] prompted the MAC collaboration to propose, in autumn 1983, the addition of a high precision vertex chamber to the MAC detector. The design utilized thin walled cylindrical drift tubes made of aluminized mylar. The device was installed in autumn 1984, immediately provided useful data, and continued to operate until March, 1986, when MAC data taking ceased. It has achieved the highest spatial resolution –35 $\mu$m– of any drift chamber used at colliders for physics results. In this paper, we describe the research and development of this chamber, its performance, and the $B$-lifetime result obtained with it.

The success of this chamber has helped convince many collaborations, including the Mark-III at SPEAR, CLEO at CESR, the upgraded TPC at PEP, AMY at TRISTAN, and JETSET at LEAR to build or propose similar devices. Indeed several features of this type of chamber are well matched to the probable conditions at the ELOISATRON or SSC: the small cell size is suited to the high rate and dense tracking environment anticipated; the simplicity and ruggedness makes a system of $10^5$ channels credible. It should be noted that the MAC vertex chamber has operated only 4.6 cm from colliding beams, and has suffered *no* degradation due to radiation damage; this augurs well for survival in the more extreme conditions of the ELOISATRON or SSC.

### Motivations and Strategy

Our initial motivation for using the thin walled mylar tubes[4,6] (often referred to as 'straws' because they are made in a spiral wrap, much like paper drinking straws) was simplicity and robustness. Problems of field wires and drift field mapping are eliminated. If a sense wire breaks, it is physically and electronically isolated from the other sense wires, so does not harm the rest of the chamber. However, there are other advantages to the use of straws. We have obtained 20 $\mu$m spatial resolution in beam tests with them, and 35 $\mu$m in our vertex chamber in use for physics results. Their small size is not only useful for the high rate environment, but aids pattern recognition in the dense regions of multitrack events. Their large, flat cathode makes straws less susceptible to some ills of radiation damage, including whisker growth and cathode coating.

Our Monte Carlo studies[7] indicated that the spacing of ionization clusters, and not diffusion, dominates the spatial resolution for drift distances as short as those in straws. This is in contrast to jet type cells, and indicated that the best strategy for high spatial resolution is to trigger the timing discriminator at the least possible ionization, instead of using the centroid in time of ionization arriving at the sense wire. To achieve a low threshold, we decided to operate the chamber at the highest possible gas gain, even in the 'self quenching streamer' mode if possible. We also decided to operate the chamber at high pressure, to reduce the spacing between ionization clusters.

Of course, a disadvantage of high gas gain is that the chamber might age quickly from beam-related radiation. We carefully designed our shielding and avoided this problem. Other disadvantages of straw chambers include: 1) the drift region close to the wire makes up a larger fraction of the active region than in jet type cells; this region *can*, but by no means *must*, have poor spatial

resolution; 2) high gas gain is not linear with ionization, possibly impeding dE/dx measurements; 3) the radial drift field makes multihit resolution difficult; 4) the matter in the straw walls causes photon conversion and multiple coulomb scattering; and 5) very long straws are hard to keep straight. None if these disadvantages appear insurmountable.

We took great care in the machining of the endplates and the placement of our sense wires, but our strategy was always to survey the positions of the wires *in situ* with tracks from Bhabha scattering events. This has proved very successful. We have established the wire positions to 10 $\mu$m in this manner.

## RESEARCH, DEVELOPMENT, AND DESIGN

### Gas Gain

Using a test straw of 6.9 mm diameter and 20 $\mu$m sense wire, we discovered that the aluminized mylar walls were photosensitive. Light from an incandescent bulb was shone on the straw wall, and caused ejection of photoelectrons, which we then used for the study of gas gain. Battistoni *et al.* have observed similar behavior in aluminum-walled streamer tubes[5] We observed that the efficiency of the cathode for photoconversion was highly dependent on the history of the straw; higher efficiencies could be induced by several seconds of high voltage discharge in the straw.

We noticed that signals from the large amount of primary ionization from the 5.9 keV X-ray of an $Fe^{55}$ source never went through the characteristic 'jump' from proportional to streamer mode. It is possible that electrostatic saturation limited the gain. In contrast, the signals from single electrons *did* go through the characteristic jump, as shown in Figure 1. In the streamer mode, single electron pulses were nearly as large as those from 5.9 keV X-rays. The stable streamer 'plateau' for single electrons lasted for 500 V in 4 atm absolute 50% Argon-50% Ethane. We found similar behavior in two gas mixtures with no organic additives: 49.5% Argon-49.5% $CO_2$-1.0% $CH_4$, with a 200 V plateau; and 50% Argon-40% $CO_2$-10% Xenon, with a very nice 900 V plateau. The limiting behavior at the high end of the plateau was photoelectric feedback from the cathode. Stable, large pulses from single electrons have been achieved in Magic Gas[8] where the addition of freon suppresses feedback from the cathode; similar gas gains have been achieved in Dimethylether[9]

Operation at high voltages where single electrons produce streamers would lead to the best spatial resolution for short drift distances, as discussed in the previous section. The noise requirements on the preamplifiers would not be stringent.

### Radiation Damage

The primary obstacle to operation at high gas gain near colliding beams is damage induced by background radiation. We conducted studies of radiation damage in a test apparatus as similar as possible to our proposed vertex chamber. In particular, we conducted the tests at 4 atm absolute pressure, and did not circulate the gas; plastics such as teflon, PVC, and epoxy were used in the test vessel. More details of our tests appear in Ref. (10).

We found a variety of Argon-Hydrocarbon mixtures, including 50% Argon-

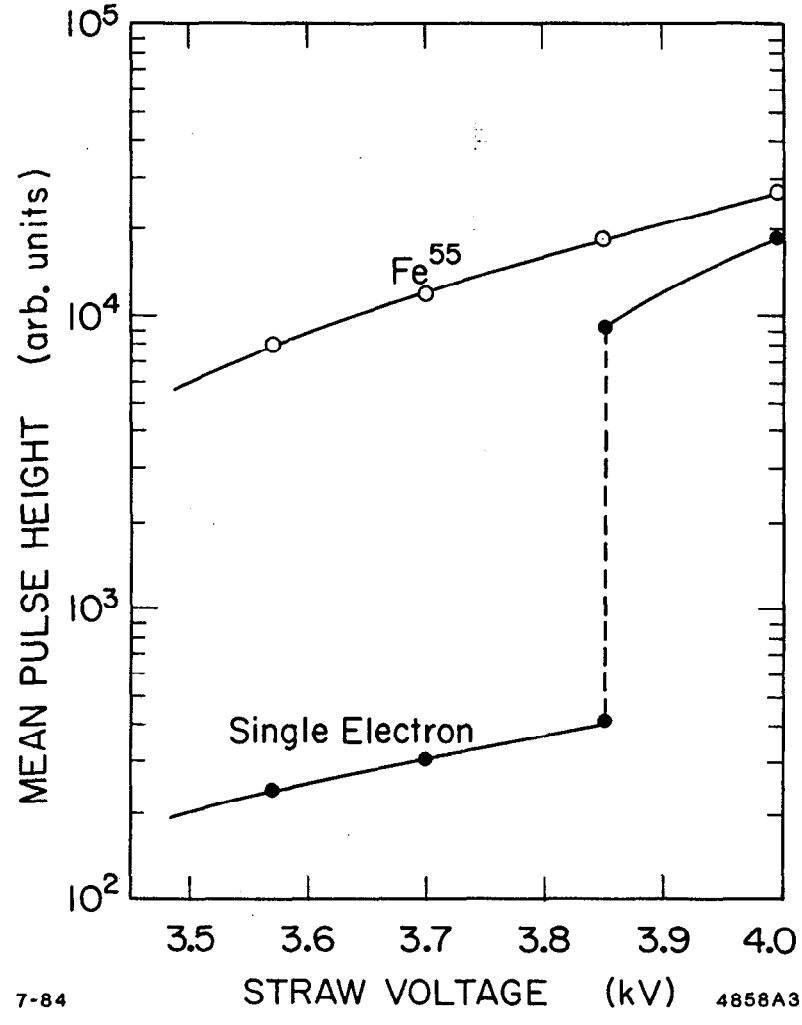


*Figure 1* Gas Gain for 5.9 keV X-rays and single electrons. Data taken with 50% Argon- 50% Ethane at 4 atm. absolute, with a 20 $\mu$m sense wire and a straw of radius 6.9 mm. The signal from $Fe^{55}$ X-rays never underwent the characteristic 'jump' into streamer mode, but the single electron signal did.

50% $C_2H_6$, 70% Argon-30% $C_4H_{10}$, and 49.5% Argon-49.5% $C_2H_6$-1.0% $H_2$ failed reliably and repeatedly at 0.05 C/cm of accumulated charge. The straw would go into continuous discharge; replacement of the anode wire restored performance, clearly indicating anode damage. We opted not to add alcohol, as this damaged the glue in the straw.

We decided that 0.05 C/cm was unacceptable, so we turned to a non-organic quencher, $CO_2$. 50% Argon- 50% $CO_2$ showed no anode damage; in fact, study of the $Fe^{55}$ X-ray spectrum indicated the anode wire became cleaner up to 0.05 C/cm accumulated charge. However, the straw failed at 0.25 C/cm accumulated charge due to disappearance of aluminum on the cathode. We hypothesized that positively charged $CO_2$ fragments attacked the cathode. We added a small

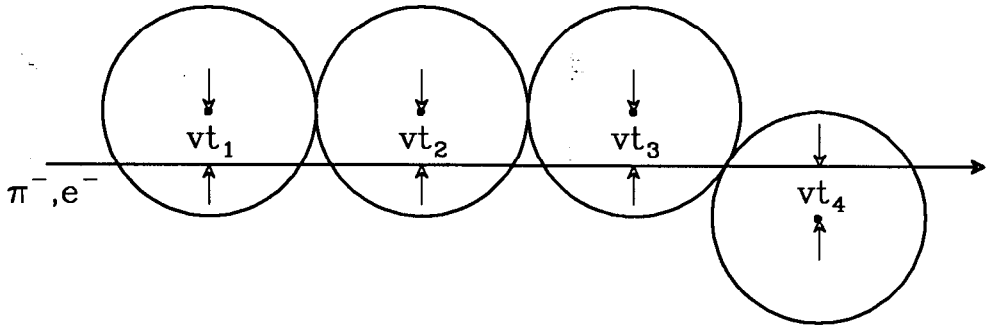


Spatial Resolution: $\Delta = t_2 - \frac{1}{2}(t_1 + t_3)$

$\sigma_W = \sqrt{\frac{2}{3}} v \sigma_\Delta$

Drift Velocity: $v \simeq 50\ \mu m/ns$

*Figure 2* Straw Arrangement in Test Beam. Electrons and pions from were supplied in the SLAC Research Yard. $v$ is the drift velocity, which was typically a constant 50 $\mu$m/ ns for the Argon-Hydrocarbon gases used. The spatial resolution, $\sigma_W$, was determined from the drift times in the first three straws. The fourth, staggered straw was useful for determining the time to distance relationship.

amount of $CH_4$ hoping charge transfer would occur, and that $CH_4$ species would cause less damage to the cathode. Only a slight improvement was observed; we settled on 49.5% Argon-49.5% $CO_2$-1.0% $CH_4$ as our operating gas. Use of Xenon rather than $CH_4$ led to a similar slight improvement in lifetime.

The aluminum layer on our mylar had a surface resistivity of 0.8$\Omega$/square, indicating a thickness of $\approx$ 30 nm. A thicker layer or aluminum, or use of a different metal, may extend the liftime or straws.

Beam Test

We conducted a beam test[6] to determine the resolutions possible with a drift chamber made of straws. A variety of high voltages, discriminator thresholds, gases, and pressures were used. An unseparated beam of 8 GeV/$c$ electrons and pions in the SLAC Research Yard was used. Four straws were arranged as shown in Figure 2. The simple geometry allowed a straightforward and systematic free determination of the spatial resolution. The spatial resolution as a function of drift distance is given in Figure 3, for a variety of discriminator thresholds. In the streamer mode at 4 kV, the spatial resolution was an average of 25 $\mu$m, *and did not degrade near the sense wire*. The data agree quite well with Monte-Carlo calculation. Figure 4 shows the spatial resolution measured for a variety of high voltages and gas pressures. Based on these test beam results, one sees that straws obtain spatial resolutions in the 25 $\mu$m regime.

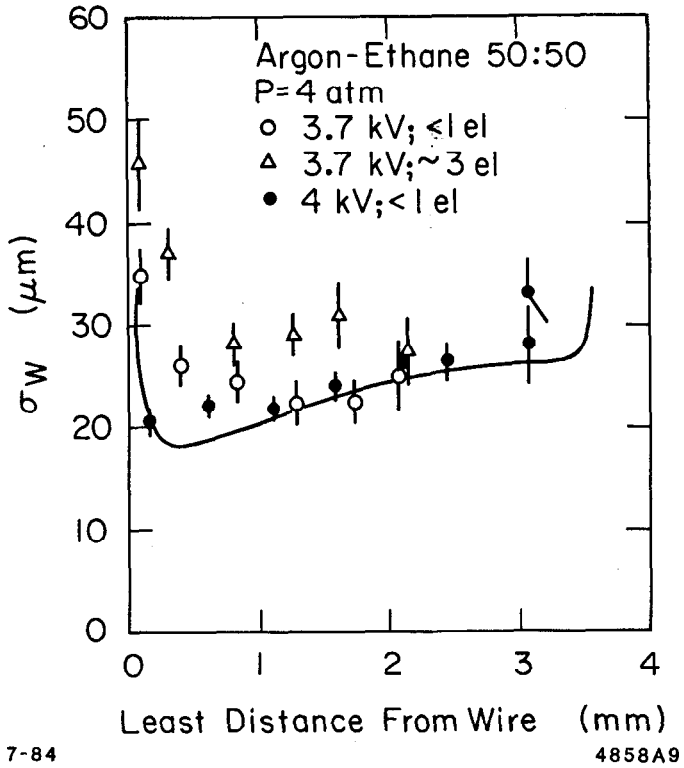


*Figure 8* Spatial Resolution in Test Beam vs. Drift Distance for a Variety of Thresholds. Absolute calibration of the thresholds were performed with a source of single electrons produced via the photoelectric effect on the straw cathode. The streamer mode was fully efficient at 4 kV for single electrons. Our Monte-Carlo calculation is shown as well.

## Design

Radiation Shielding. At the beginning of PEP operation, the MAC detector ran for a short time with a 3.15 cm radius beam pipe, and minimal shielding was employed. From this experience, we deduced that the primary radiation background came from off-energy electrons that were overfocussed by the 'low-beta' quadrupoles into the beam pipe and tracking chamber. Another important background source was synchrotron radiation, both from the 'soft bend' dipole and the low-beta quad.

We designed a close-in collimator to suppress these backgrounds. The collimator was a tantalum annulus of 2.8 cm inner radius and 0.8 cm thickness, placed 60 cm from the interaction region. Shielding of heavimet, a sintered tungsten material, surrounded the collimator to absorb electromagnetic showers. The location and dimensions of the collimator were chosen to allow sufficient room for this shielding, and to shield the vertex chamber from direct particle and photon trajectories from the soft bend and low-beta quad magnets. Figure 5 shows the shielding and these trajectories. A 75 $\mu$m titanium liner, placed inside the beampipe to attenuate the $\approx$ 10 keV fluorescence of tantalum by a factor of $\approx$ 30, completed the shielding.

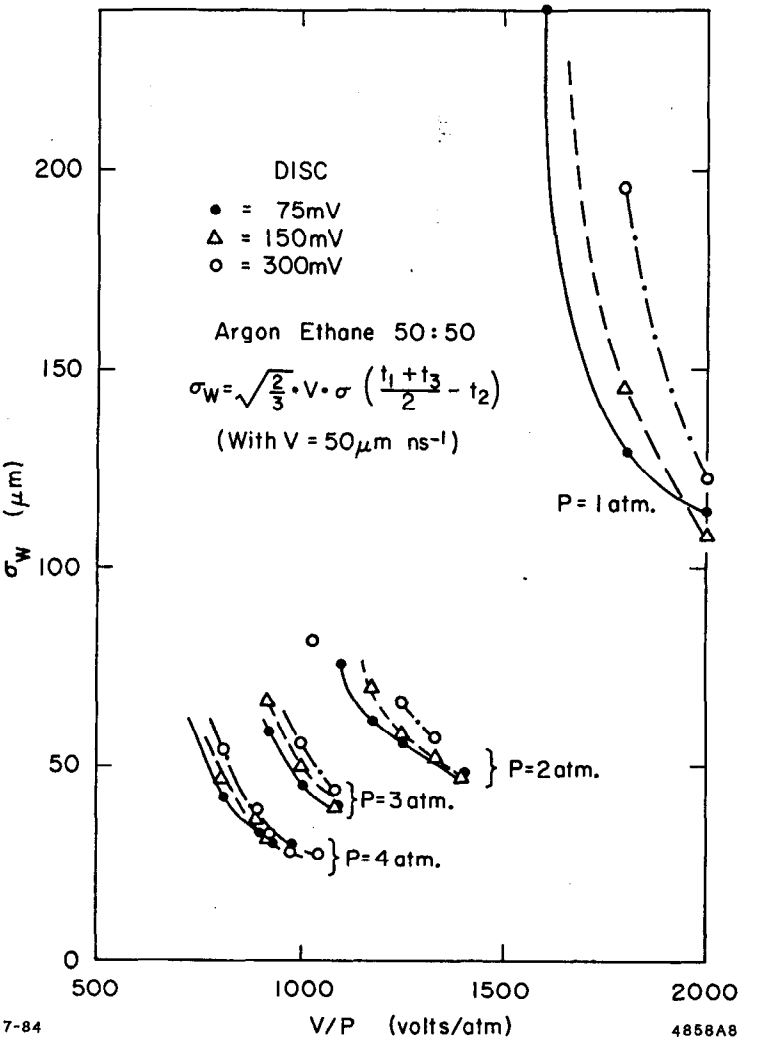


*Figure 4* Spatial Resolution in Test Beam For a Variety of High Voltages, Pressures, and Discriminator Thresholds.

The heavimet occluded the low angle electron veto counters previously installed for the MAC search for $e^+e^- \rightarrow \gamma +$ *weakly interacting particles*.[11] To maintain this search, an annulus of BGO was placed between the heavimet and interaction region. The dense BGO was read out with compact photodiodes;[12] a well matched combination for such a cramped situation. This was the first application of this technology in an operating colliding beam experiment.

Beampipe and Pressure Vessel. The beampipe was 0.11 cm thick beryllium, brazed to aluminum tubes at its ends. The aluminum tubes were in turn welded to the pressure vessel endplates, which were an explosion welded bimetal of aluminum and stainless steel. The remainder of the pipe was stainless steel. The outer wall of the pressure vessel was a 2.54 mm aluminum tube, also welded to the bimetal endplates. The outer wall carried the mechanical load of the beampipe and shielding. I-beams place vertically above and below the beampipe carried

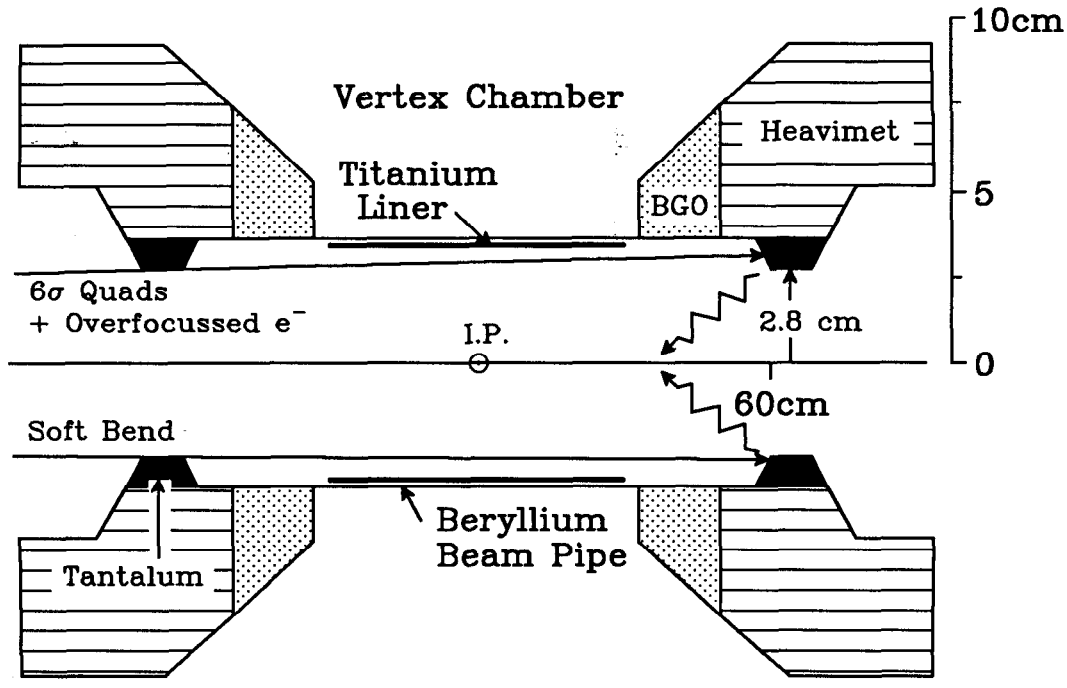


*Figure 5* Shielding Configuration. The tantalum close-in collimators and surrounding heavimet shielding protected the vertex chamber from off-axis electrons, and off-energy electrons overfocussed by the nearby low-beta quadrupoles. The collimators also shadowed the vertex chamber from direct synchrotron radiation from the soft bend and low-beta quad. The titanium liner absorbed the $\approx$ 10 keV fluorescence from the tantalum. The remaining background were $\approx$ 25 keV synchrotron light from the low-beta quad, that was scattered off the tantalum.

the load on either side of the vessel.

The pressure vessel was distinct from the vertex chamber. The coaxial signal cables from the chamber were potted in epoxy plugs that were captured in the endplates and sealed with O-rings.

Chamber. The straws were strung on a spool that consisted of a 0.076 cm thick, extruded beryllium tube, to which 1.6 cm thick aluminum endplates were glued. Holes were precision reamed in these endplates to accept the endplugs of the straws. The endplate layout is shown in Figure 6. There are six radial straw layers, arranged in three pairs. The inner layer of each pair is close packed in azimuth. The outer layer contains the same number of straws as the inner, but is staggered one half cell in azimuth. The stagger resolves the left-right ambiguity in the straws.

The straws themselves had an inner diameter of 6.9 mm. The wall consisted of a double wrap of 50 $\mu$m mylar, each layer coated on one side with 0.8$\Omega$/square. surface resistivity aluminum. The conductive layers faced inward and outward. The pitch angle of the spiral wraps was 28°.

The end-fitting design is shown in Figure 7. An aluminum collar was glued with conductive epoxy to the straw inner face, trapping a Delrin (acetal) plastic

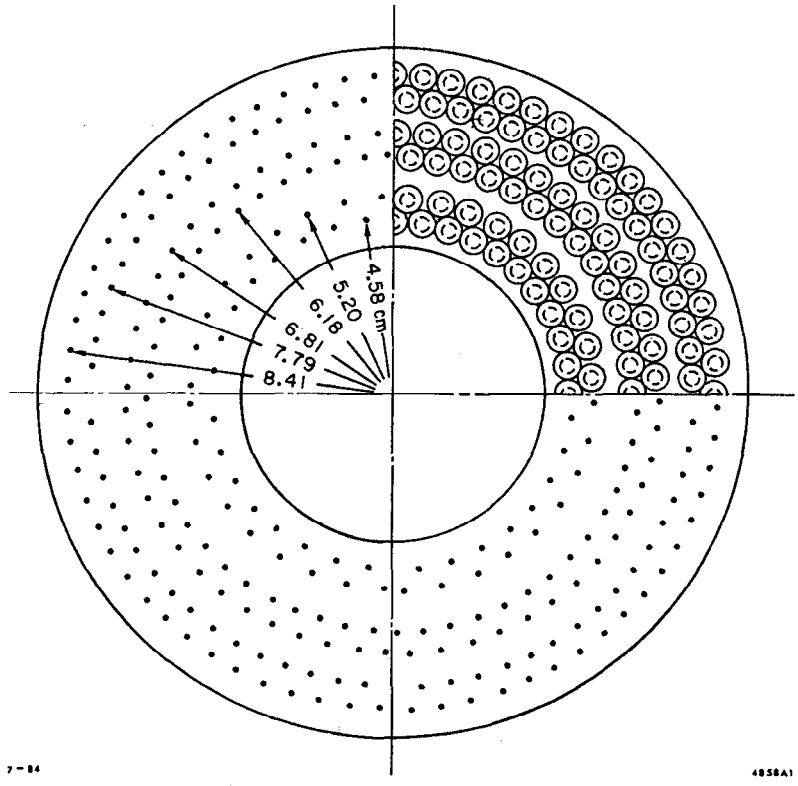


*Figure 6* Spool Endplate Layout, Showing Placement of Straws in Radius and Azimuth.

plug. The plug performed several functions. First, it insulated the high voltage on the sense wire from the ground of the endplate and straws. For this reason, virgin Delrin, Delrin that was not reformed from old pieces, was used, to avoid cracks and crevices that lead to high voltage breakdown. Considerable trial and error lead to the shape of the plug inside the straw, in order to avoid edge breakdown at extremely high voltages. Second, the plug provided a means to apply tension once the straw was mounted between the endplates. The threaded tip of the plug allowed a nut to apply tension when tightened. Third, the plug provided a seat for the feedthrough that held and positioned the sense wire. Last, the plug provided a conduit for gas flow through the straw, via two channels cut lengthwise on its outer radius. The 30 $\mu$m gold-tungsten sense wire was threaded through the 100 $\mu$m hole of a tempered stainless steel tube, or feed through, which was crimped to capture the wire.

Signal Processing. Figure 8 shows the electronic layout of the vertex chamber and associated electronics. The sense wires were operated at positive high voltage, and one end was terminated through a standoff capacitor and a resistor. The other end was connected to 19 meters of RG179B, a 75$\Omega$, teflon insulated, miniature coaxial cable. This coaxial cable provided high voltage, and carried signals to preamps that were located away from the detector.

We used the LABEN 5242 preamplifier, a hybrid optimized for fast rise time

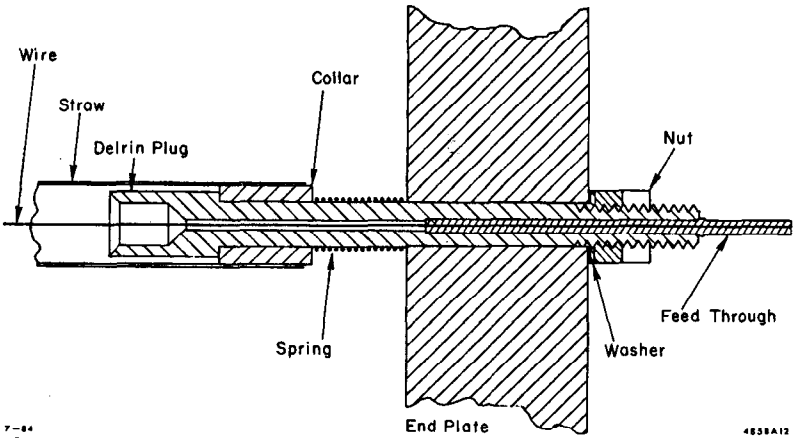


*Figure 7* End-fitting Design for Straws. See text for more details. The collar contacted the endplate on one end of the straw; on the other, the spring made electrical contact.

and low noise. In retrospect, this preamp was better matched to sources with impedance higher than our signal cables.

Our discriminator circuit utilized the Plessey SP9687 dual comparator. Each discrimator channel used two comparators, one set to a low threshold, and one high, as shown in Figure 9. The discriminator output was fed to our time-to-voltage converters, or TVC's. These circuits demonstrated $< 300ps$ timing resolution in bench tests.

Gas System. The gas system was designed to maintain constant density in the chamber while allowing gas flow. Figure 10 shows the gas circuit of the final design. The gas pressure was maintained by mechanical regulators. These proved quite reliable, but were sensitive to ambient thermal variations, necessitating thermal isolation. Flow was maintained by a vacuum pump on the output of the system, which eliminated variation from atmospheric pressure fluctuation. The temperature of the chamber was maintained nearly constant by the cooling system of our solenoid; no effect of heating from the beam was observed.

This system maintained the gas density constant with an rms density of 0.8% over one week. The rms variation of the time to distance relationship contributed by this was a maximum of only 14 $\mu$m, at the straw wall. An electrical control system would seize control of the pressure if the density wandered outside $\pm 0.75\%$; this only occurred once in the operation of the chamber. Adjustment of the mechanical regulators for long term drift was made several times per week.

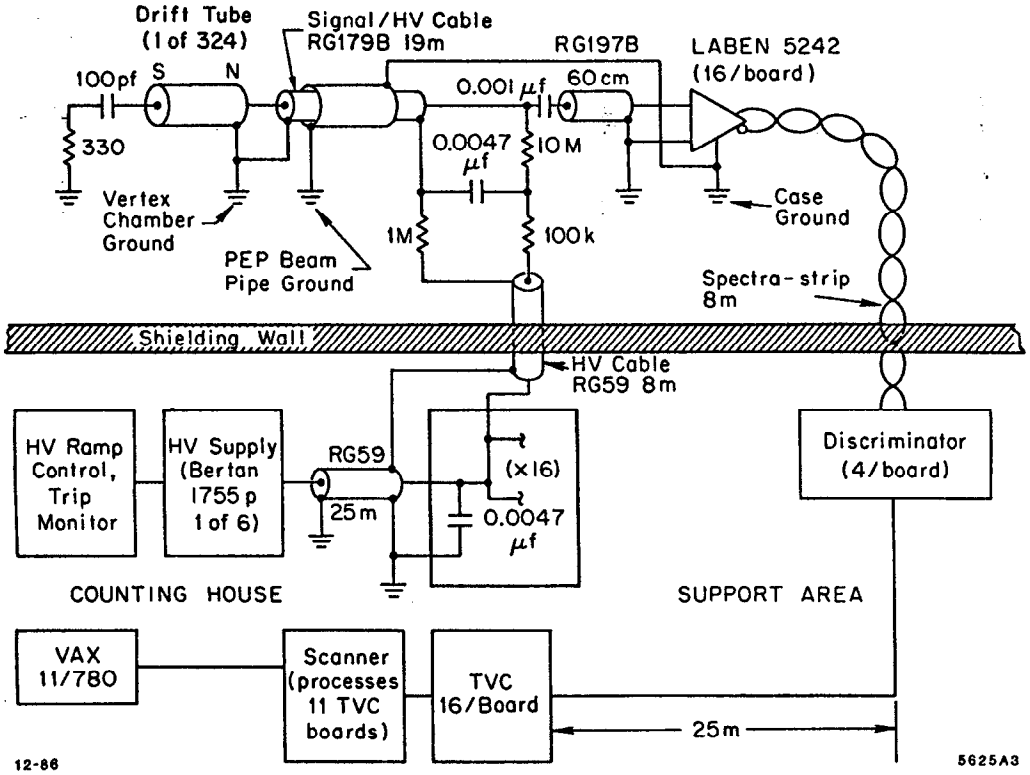


*Figure 8* Electronic Layout of the Vertex Chamber. Straws are terminated in approximately their characteristic impedance at one end; signals go from the straw's other end, through 19 meters of coaxial cables to the preamplifiers, then to the discriminators and finally the TVC (time to voltage) drift time measuring system.

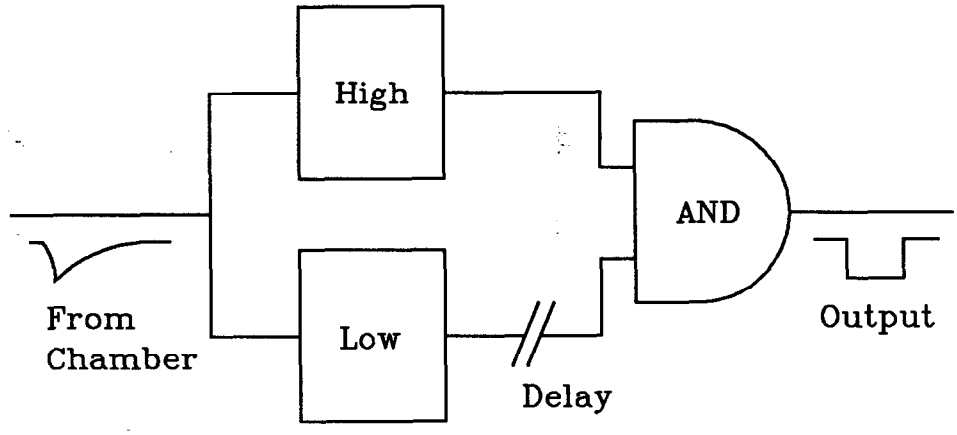


*Figure 9* Principle of Discrimator Circuit. The low level output was delayed, so typically they reached the AND gate after the high level. Hence, the low level comparator controlled the timing of the output, but small pulses that did not fire the high level comparator were suppressed.

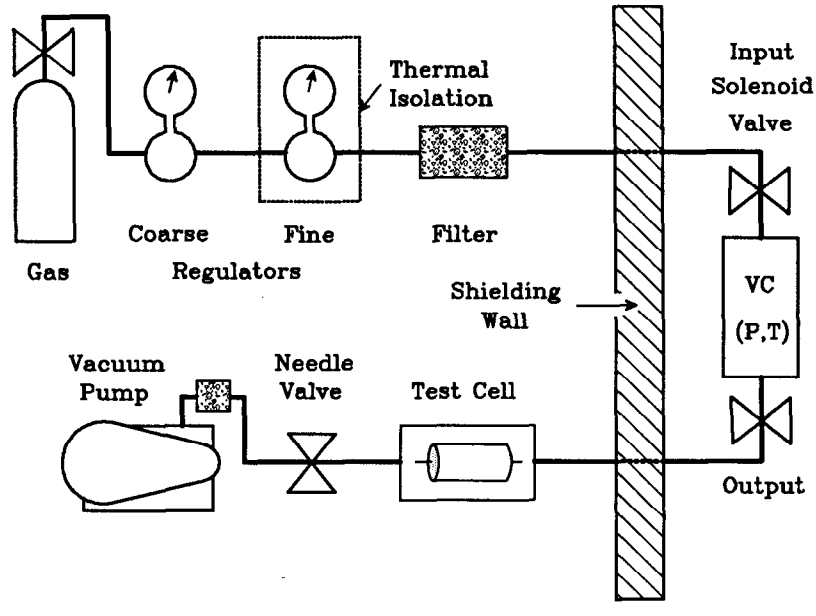


*Figure 10* Gas System Circuit. Pressurized gas from cylinders flowed through Poly-Flo tubing to the vertex chamber, then back through a test chamber and a vacuum pump, which vented to the atmosphere. Absolute pressure was maintained by a pair of mechanical regulators on the cylinder output, and a needle valve on the output controlled the flow rate. Pressure and temperature were monitored in the vertex chamber (VC); if the density in the chamber drifted outside limits an electrical circuit could regulate the density via the solenoid valves.

## VERTEX CHAMBER

### Vertex Chamber Performance

Electronics. Refer to Figure 8 for the electronic layout of the vertex chamber and associated electronics. The electrical ground of the vertex chamber was insulated from the ground formed by the PEP beam pipe, to suppress pickup from the image currents of the beam itself. No pickup from this source was observed at the level of white noise from the preamplifiers. However, the long signal cables between the chamber and the preamplifiers proved susceptible to electromagnetic interference in the 1-100 MHz regime. Their susceptibility was reduced substantially by isolating both their center conductor and shield with 1-10 MΩ resistors from the high voltage supply cables. The dominant source of interference was the system for measuring drift times in the vertex chamber (VC), the time to voltage converters (TVCs). Moving these from 10 meters to 30 meters from the preamplifiers reduced the total pickup to approximately the level of the white noise of the preamps.

The long cables limited the 10-90% rise time at their output to 4 ns, and attenuated signals from the chamber by 15%. The output slew rate of the preamps was 90 mV/ns, yielding a 10-90% rise time of 8.0 ns for pulses from $Fe^{55}$ sources in the chamber. The white noise of the preamps was 2.0 fC at their input with cables attached, 0.6 fC without. The low level of our discriminators was set at 6 fC input to the preamps, which corresponded to 30 mV at their output. Slewing and noise contributed less than 0.15 ns to our timing resolution.

TVC channels were calibrated with a CAMAC controlled delay generator. The delayed calibration pulse was injected at the preamplifier input, into half the channels at a time. For each channel, the delay was fit as a quadratic function of the voltage output from the TVC. The non-linearity contributed only 0.5% to the calibration. This calibration was performed 8 times over the 17 months of data taking.

The channel by channel pedestals had a standard deviation of 15 ns; this was governed by the variability of a CMOS switch in the TVC circuit. Over the data taking period these pedestals were stable to 1.3 ns. The slope term in the quadratic fit was far more reproducible from channel to channel, varying only 1.3%; this was governed by one resistor and one charging capacitor. The drift was only 0.5% in these slopes. Figure 11 shows the actual distributions of the offsets and slopes.

The calibration reproduced input delays to better than 0.5 ns. During data taking, four spare channels were fed fixed delays; these indicated that the system achieved a timing resolution over a typical two hour data taking run of 250 ps.

The combined effect of 1)slewing in the signal cables; 2)noise in the preamplifiers; and 3)resolution of the TVC system produces a timing resolution of $< 300$ ps. The maximum drift velocity in the vertex chamber itself was $100\,\mu$m/ns. Therefore the degradation in spatial resolution from purely electronic sources was $< 30\,\mu$m.

Operating Point. The high voltage and threshold at which the chamber was operated was a compromise between spatial resolution and radiation damage considerations. As discussed in earlier, for the short drift distances in our cells,

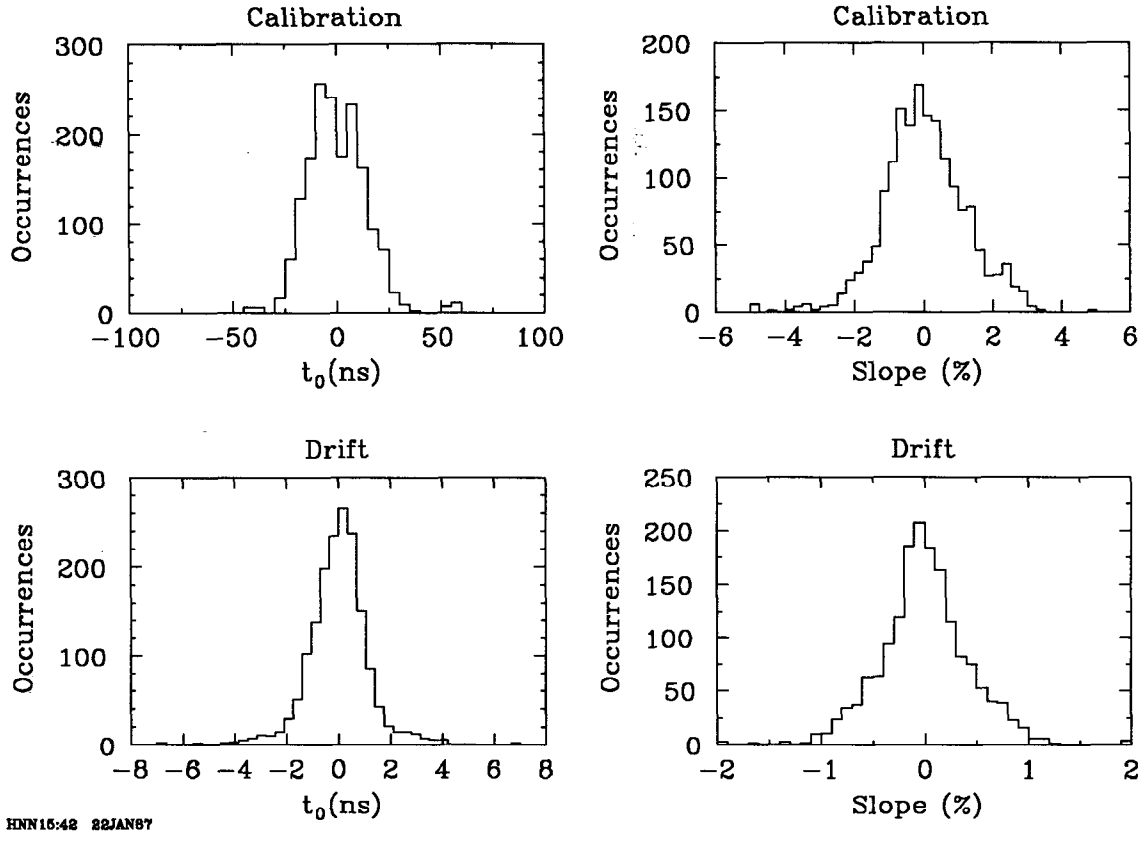


*Figure 11* Fitted constants in the TVC system. The top plots are distributions of the timing pedestals and slopes. The bottom plots give the variability of these constants over the 8 recalibrations done during the 17 months of data taking.

triggering on the first arriving electron was desirable. The observed charge for various high voltages appears in Figure 12. At 3900 V, our threshold of 6 fC was very near the most probable signal for a single electron. Synchrotron X-rays were the dominant source of current drawn in the chamber. Approximately two random hits per beam crossing occurred in the chamber, causing a current of 3-5 nA/cm to be drawn in the innermost layer, for a high voltage of 3900 V. Higher voltages put the chamber in danger of accumulating more than 0.2 C/cm charge in the innermost layer, so we operated at 3900 V. In retrospect, we were slightly conservative; the innermost layer accumulated only 0.03 C/cm over the entire data taking period.

The two random hits per beam crossing interfered in no way with our track finding procedure. Electronic cross talk did not limit our ability to maintain a low threshold: studies with Bhabha events indicated that electronic cross talk produced $< 0.1\%$ of the hits in five of the six layers. However, knock-on electrons did produce hits in the cells immediately neighboring a cell penetrated by a track 1-2% of the time.

Off–line calibrations

We performed off–line calibrations of wire positions, drift timing constants,

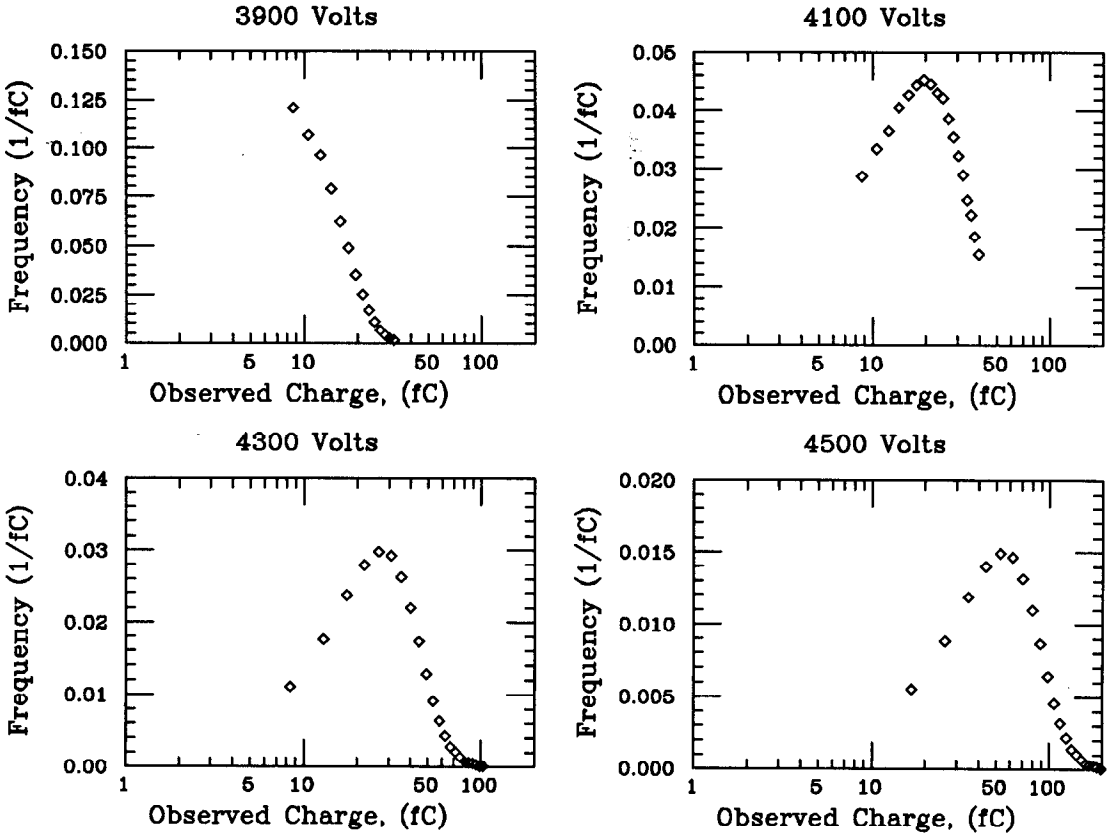


*Figure 12* Single Electron Gain. The four plots are for different high voltages applied to the sense wire. These data were obtained with a test straw identical to those used in the vertex chamber. An incandescent light produced single electrons via the photoelectric effect on the straw cathode. Not shown are the very large charges due to self quenching streamer formation which were approximately 500 fC. Few single electrons initiated streamers at 3900 Volts, but most did at 4500 Volts. The spectra are not shown below 8 fC where amplifier noise begins to dominate. The gas mixture was 49.5% Argon, 49.5%$CO_2$, 1.0%$CH_4$, at an absolute pressure of 4 atm.

the time to distance relationship, and drifts in these quantities. Bhabha scattering events proved very useful for this purpose due to their simple topology. The use of Bhabha scattering events is by no means mandatory. Any sample of tracks free of bias from pattern recognition could have been utilized. Bias can occur, for example, in dense regions of multihadron events, when two tracks pass through the same cell but only one is recorded.

Our calibration techniques require existing programs to link hits into tracks and to fit the track parameters. The programs used to do this are described in and reference (13).

Global Alignment. For a description of our tracking parameterization, see the appendix. The VC measured only the three parameters that describe the track in the x-y plane. Of these three, only two were well measured, $\delta_{0vc}$ and

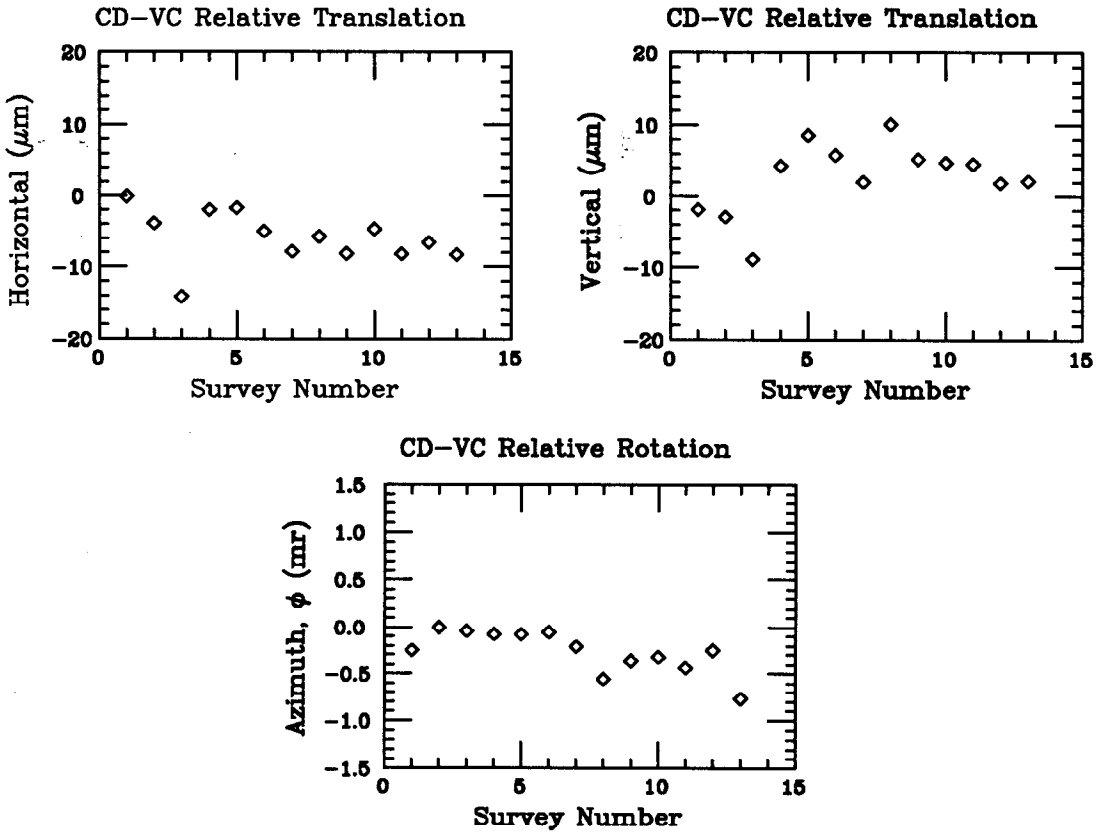


*Figure 13* Drift of Global Alignment Parameters. The global alignment of the VC relative to the CD was done 13 times during the 17 months of data taking. The drift of the two translation parameters are shown in the upper plots, and the drift of the relative azimuth in the lower. The alignment was stable to 10 $\mu$m.

$\phi_{0vc}$. Our existing central drift (CD) chamber extended from 12 cm to 45 cm in radius, and had stereo layers, so it measured all five helix parameters. Systematic comparison of $\delta_{0vc}$ and $\phi_{0vc}$ with $\delta_{0cd}$ and $\phi_{0cd}$ as a function of $\phi_{0cd}$, $\theta$, and $z_0$ allowed determination of the five relevant parameters that describe the relative global orientation of the VC and the central drift chamber.

These five parameters were measured 13 times over the course of data taking. Figure 13 shows the stability of the three most important over these measurements. The horizontal and vertical translations were stable to 10 $\mu$m.

Time to Distance Calibration. The gas used in the vertex chamber, 49.5% Argon, 49.5% has a drift velocity approximately proportional to the applied electric field. In a cylindrical geometry, this implies the drift distance $r$ and the drift time $t$ are related by $r \approx \sqrt{t}$. This simple relationship provided an initial guess for our time to distance function.

We improved the initial guess with the following procedure. Tracks in Bhabha scattering events with 4-6 hits in the VC and 7-10 out of 10 possible hits in the CD were chosen. A VC hit waseliminated, and the remaining VC and CD hits were

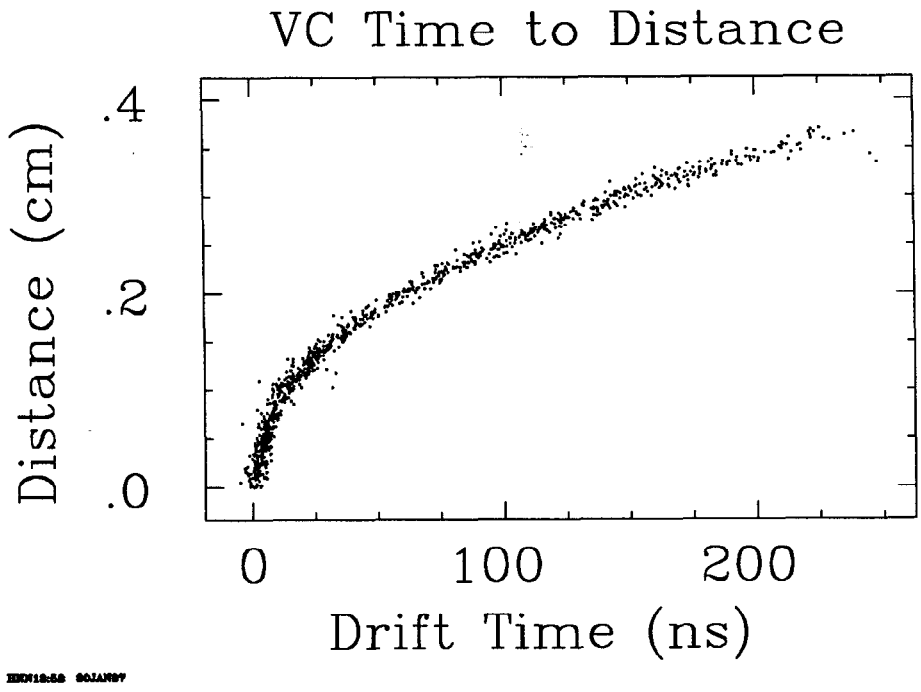


*Figure 14* Time to Distance Relationship. The drift time is that measured in a cell of the VC, $t_{meas}$. The drift distance is obtained by dropping that cell from the track fit, then predicting the drift distance in the missing cell. In this manner the cell's 'pull' in the track fit is avoided. A fit is made to data like that above to obtain the functional time to distance relationship.

used in a new track fit. This new fit was used to predict the drift distance, $r_{pred}$, in the eliminated VC cell. Errors in the initial time to distance relationship tend to cancel in $r_{pred}$. We give a scatter plot of $r_{pred}$ as a function of the measured drift time, $t_{meas}$ in in Figure 14. The $r_{pred} \propto \sqrt{t_{meas}}$ character is evident. We fit data such as that in Figure 14 to obtain the improved time to distance relationship, $r(t)$, or its inverse, $t(r)$. Fitting $r_{pred}$ as a function of $t_{meas}$ or vice versa yield systematically different results for short drift distances, because no drift distances are defined as negative. Furthermore, the large slope of $\sqrt{t}$ near $t_{meas} = 0$ makes fitting $r_{pred}$ as a function of $t_{meas}$ difficult. Fitting $t_{meas}$ as a function of $r_{pred}$ proved to require fewer parameters and converged more easily. Cubic splines or orthogonal polynomials were used as fitting functions. The time to distance relationship converged to within 10 $\mu$m after one iteration of improvement. The relationship was evaluated five times over MAC data taking, usually after slight changes in gas mixture.

To account for drifts in timing, gas density, and electronics, run by run corrections were applied to the time to distance relationship. A typical run lasted 90 minutes and yielded 100 Bhabha scattering events for calibration. The drift time actually used in the time to distance relationship, $t$, was computed from

$$t = t_{0rr} + s_{rr} t_{meas}$$

where $t_{0rr}$ and $s_{rr}$ are the run by run timing offset and slope. These are found

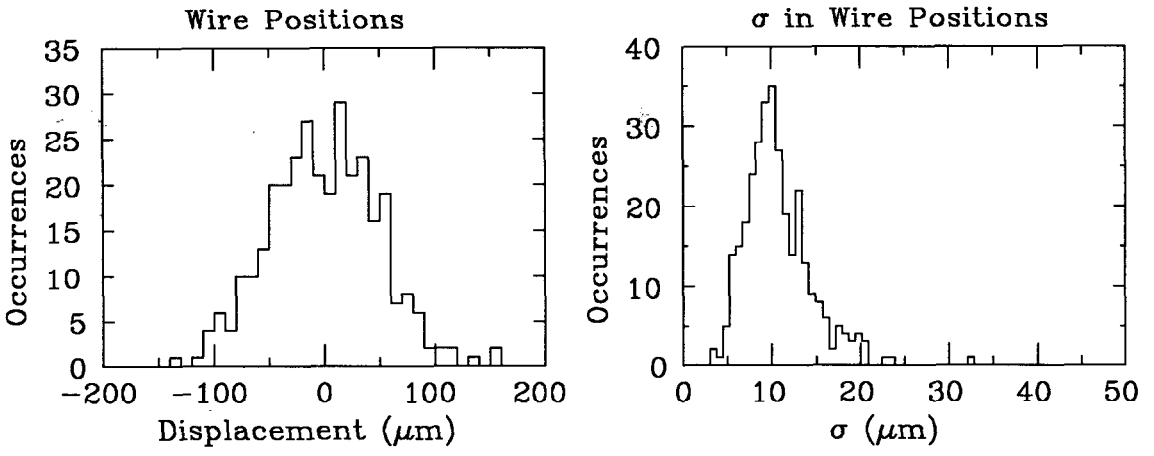


*Figure 15* Sense Wire Positions. The histogram on the left gives the wire offsets in azimuth as obtained in the channel by channel calibration. The accuracy of wire placement was controlled by the size of the hole in the crimp pins that capture the sense wire, and the pins' tendency to bend slightly. This calibration was repeated 13 times; the histogram on the left is the standard deviation of each wire's offsets among the 13 calibrations. It indicates that the calibration procedure found the wire positions to $\approx 10\,\mu$m accuracy.

using a procedure very similar to that used to extract the time to distance relationship. Typically $t_{0rr}$ could be measured to an accuracy of .2 ns and $s_{rr}$ to 2 %. $t_{0rr}$ remained stable for weeks, then would suddenly shift, usually due to a power failure or changes in PEP timing. The slope term was very stable, reflecting the stability of the gas density.

Channel by Channel Calibration. The timing constants and physical positions of each cell were calibrated offline. The procedure was similar to that used to obtain the time to distance calibration. The residuals $\delta r = r_{pred} - r(t_{meas})$ and $\delta t = t(r_{pred}) - t_{meas}$ were fit for each cell with four constants:

1. An offset in time, $t_0$.
2. An offset in distance, in the azimuthal direction, $d_0$.
3. A slope in time, $s$.
4. A tilt in $z$, the axial direction.

$d_0$ and $t_0$ effect $\delta r$ with opposite signs on opposite sides of the sense wire. In a typical calibration, 100 runs were used, corresponding to $6\,\mathrm{pb}^{-1}$ of integrated luminosity. This yielded approximately 150 residuals in each of the 324 cells. The largest correction was $d_0$, appearing in Figure 15. The calibration was performed 13 times. The standard deviations of $d_0$ for each cell over the 13 measurements also appear in Figure 15, indicating a reproducibility of 10 $\mu$m.

The channel by channel calibrations were made in a single pass through Bhabha scattering data. The improvement in spatial resolution due to the calibration was then immediately known via the multivariate analog of the relation-

*Table 1* Contributions of Survey Terms. These are the contributions to the *uncorrected* spatial resolution that may be attributed to the various survey corrections. The tilt in $z$ indicates a deviation of the ends of the sense wires from their average position of 38 $\mu$m.

| Correction | Contribution ($\mu$m) |
|---|---|
| $t_0$ | 45 |
| $d_0$ | 49 |
| $s$ | 20 |
| tilt in $z$ | 11 |

ship:

$$\sum_{i=1}^{N}(x_i-\overline{x})^2=\sum_{i=1}^{N}x_i^2-N\overline{x}^2$$

Use of orthogonal polynomials as fitting functions allowed straightforward isolation of the contribution of the various constants. Table 1 gives the importance of each of the constants.

The miscalibration of a channel in the vertex chamber 'pulls' the track fit and therefore can induce an apparent miscalibration in of channels in other layers. This coupling was not explicitly accounted for in our calibration procedure. The offsets in azimuth between layers tend to reduce the importance of this effect. Further, when we iterated the calibration procedure we found the constants to converge within one iteration to 10 $\mu$m of their value after three iterations.

Certain correlations between distant cells were found to occur. For example, the initial channel by channel calibration resulted in a slight uniform translation of all cells by an equal distance in the azimuthal direction. This created the appearance that the tracks in Bhabha scattering events were tangent to a circle centered on the geometric center of the chamber. The effect was eliminated by constraint of the two tracks in a Bhabha event to have equal but opposite distances of closest approach to the geometric center of the chamber. This constraint was made only for the track fits used to determine the calibration constants. Similar distortions in the mean acollinearity and momentum difference were observed and suppressed. In general, correlations between distant cells are not necessarily well constrained in our cell by cell calibration procedure. However, spurious correlations are easily removed by constrained fitting of tracks, or by constraint of the final survey constants.

## Pattern Recognition

Algorithm. Track segments were obtained by independent pattern recognition programs in the CD and the VC. The CD algorithm was complex, due to the presence of stereo layers and non-negligible track curvature.[13] The VC algorithm was simpler, because tracks are approximately straight lines in the VC.

*Table 2* Vertex Chamber Efficiency.

| Events | VC Efficiency |
|---|---|
| Bhabhas | $0.994 \pm 0.001$ |
| Taus | $0.982 \pm 0.003$ |
| Multihadrons | $0.939 \pm 0.001$ |

We regard the six layers of the VC as three double layers for the first step of pattern recognition. Because of the overlapping, regular geometry of the VC double layers, the drift distances $r_1$ and $r_2$ for hits produced by a radial track are related by:

$$r_1 + \frac{R_1}{R_2} r_2 \approx r_0 \qquad [3.1]$$

Here $R_1$ is the radius of layer 1 or the double layer, $R_2$ that of layer 2, and $r_0$ the straw radius. Pairs of hits in double layers were associated if they met [3.1] within 200 $\mu$m. Random associations were thereby suppressed, with little loss of real tracks. Most loss of real tracks occurred for very low momentum tracks or tracks from very long lived species, such as $K^0$s and $\Lambda$s. The ambiguity of which side of the sense wire the track passed is resolved by [3.1] in most cases.

Associated pairs in the three double layers were then linked based on their agreement in azimuth. A straight line fit was made to the resulting set of hits and drift distances. The straight lines found in the VC were then compared to and matched with tracks found in the CD. Unmatched CD tracks were extrapolated into the VC and a search made for VC hits. A weighted, least squares fit was performed to both the VC and CD hits and drift distances. VC hits were assigned weights based on the measured resolution as a function of drift distance (Figure 19). Multiple scattering was accounted for by allowing partially constrained kinks at the beam pipe, the boundary between the VC and CD, and at fixed locations within the chambers. A final search was made for hits along the track fit, and .1% of the VC and CD hits were dropped due to large residuals.

Considerable effort was expended scanning graphical representations of events and interrogating the pattern recognition programs to tune its decisions. After some optimization of cuts, results at least as good as those from scanning were achieved.

Efficiency. Since the CD and VC are in one sense redundant devices, it was possible to measure the efficiency of the VC by using a sample of tracks well measured in the CD. Sources of inefficiency include dead cells, overlap of particle trajectories, and inadequacy of the track finding algorithm for particles with low momentum or very large impact parameter.

We define well measured tracks in the CD by four requirements: 1)ten hits from the CD must be linked to the track, 2)$z_{0cd} \leq 5$ cm., 3)$\theta \leq 20°$, and 4)$\hat{\chi} \equiv \sqrt{2\chi^2} - \sqrt{2n_D - 1} \leq 4$. Table 2 gives the efficiency for well measured CD tracks

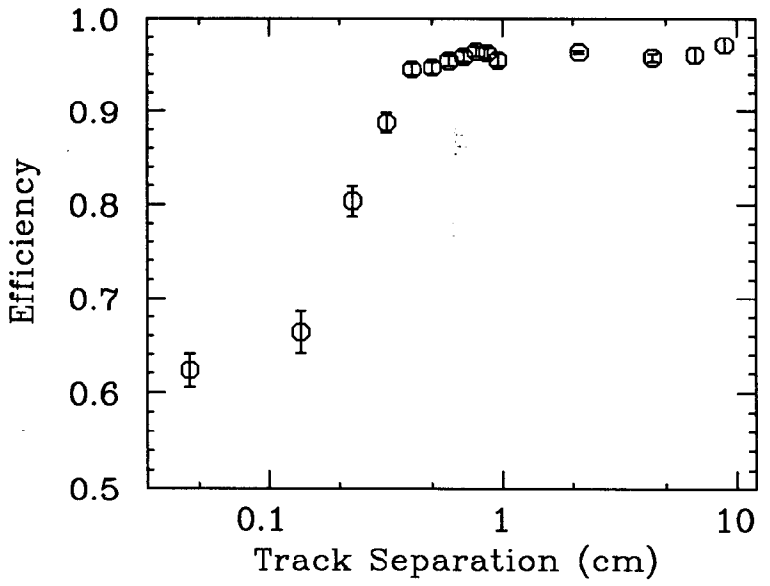


*Figure 16* Effect of Track Overlap on VC Efficiency.

to link to $\geq 3$ VC hits. The Bhabha efficiency was determined from $2\,\mathrm{pb}^{-1}$ of integrated luminosity, tau lepton and multihadron efficiencies from $94\,\mathrm{pb}^{-1}$.

Track overlap was a source of inefficiency in the VC in multihadron events. If two tracks were separated by less than the diameter of a straw, 6.9 mm, they could leave only one hit in a layer of the VC. The staggering of VC layers usually prevented this phenomenon from happening in every layer. Double-hit electronics probably could not eliminate it, because the drift field for straws is radial. Figure 16 shows the efficiency for well measured CD tracks to link to $\geq 3$ VC hits as a function of VC track separation. The VC track separation is the minimum distance in the azimuthal direction from the well measured track to the nearest CD track, within the VC boundary. The efficiency was near 50% for small separation, indicating one track of the overlapping pair was found in the VC. For large separations, the efficiency was better than 96%.

The VC track finding algorithm was most efficient for straight tracks coming from the beam centroid. The efficiency for CD tracks with VC track separation greater than one straw diameter is shown versus momentum in Figure 17. The efficiency was $\geq 90\%$ above $200\,\mathrm{MeV}/c$. Tracks softer than $500\,\mathrm{MeV}/c$ had an error in impact parameter due to multiple scattering in the beam pipe equal to their error due to chamber resolution. Since the multiple scattering error scales as $1/p$, tracks with $p < 200\,\mathrm{MeV}/c$ contribute little information to lifetime measurements. Figure 17 also exhibits the efficiency for the same tracks versus impact parameter itself. Typical impact parameters of particles from $B$-meson decay are $300\,\mu\mathrm{m}$, and the VC efficiency is flat and $\geq 96\%$ to some ten times this value, 3 mm. We conclude that linking efficiency effects lifetime measurements very little.

Well measured tracks in the VC can be used to measure the efficiency of the CD. Defining a well measured track as one with six hits in the VC, $0.932 \pm 0.001$ are matched with tracks having six or more hits in the CD, and $0.798 \pm 0.001$

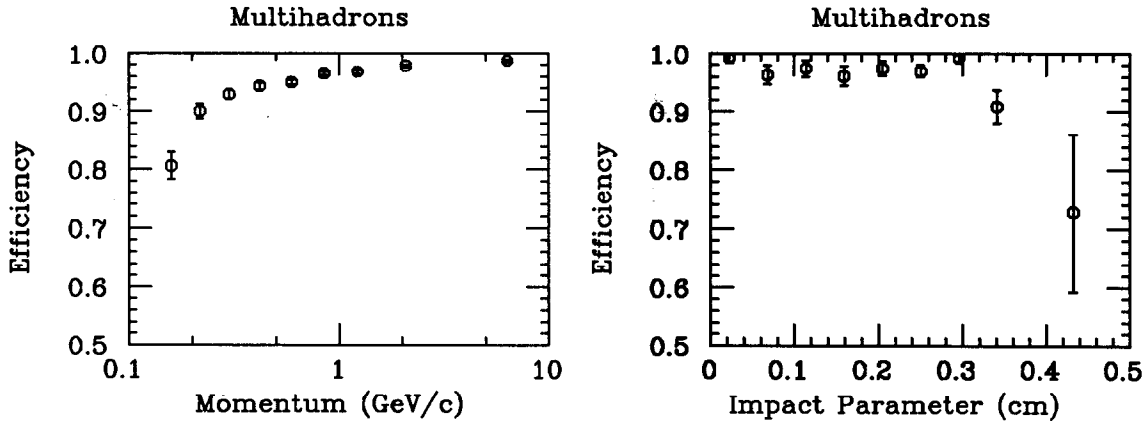


*Figure 17* VC Efficiency for Various Momenta and Impact Parameters.

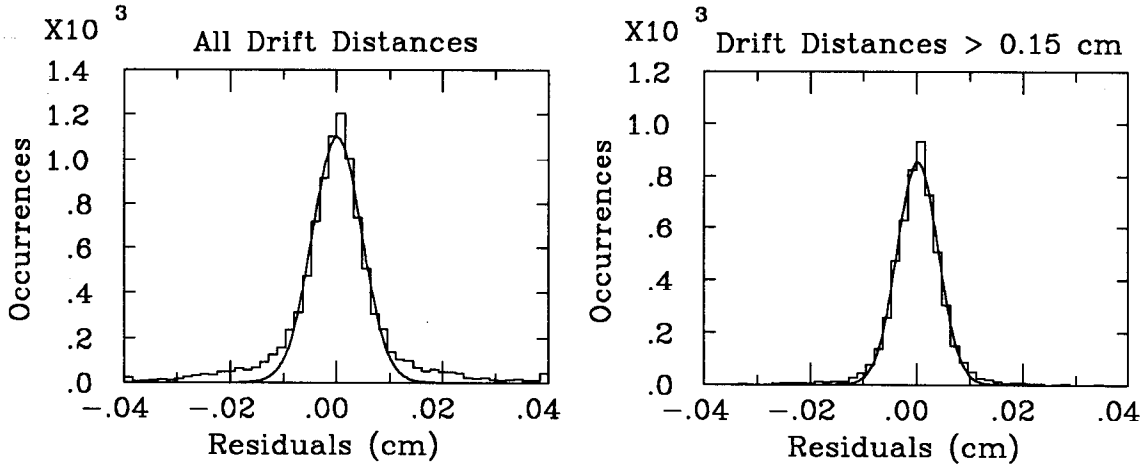


*Figure 18* VC Residuals. The hit was *removed* from the track fit in these data. Residuals for all drift distances are on the left, where the fitted gaussian has $\sigma = 45\,\mu$m. On the right, only data from distances $> 0.15$ cm; the fitted gaussian has $\sigma = 38\,\mu$m. As discussed in the text, these data *overestimate* the spatial resolution of the chamber.

are matched to tracks having seven hits or more.

Observed Resolutions

Spatial resolutions were measured using residuals from the track fit. If the VC hit used to measure the residual is left in the track fit, the resulting residual distribution is systematically narrower than the true residual distribution, due to the pull of the hit in the fit.[14] Conversely, if the hit is removed from the fit the distribution is wider then the true distribution, due to interpolation error in the track fit. The size of the bias is almost equal in these two cases, but opposite in sign. Figure 18 displays the residuals from Bhabha scattering events, where VC

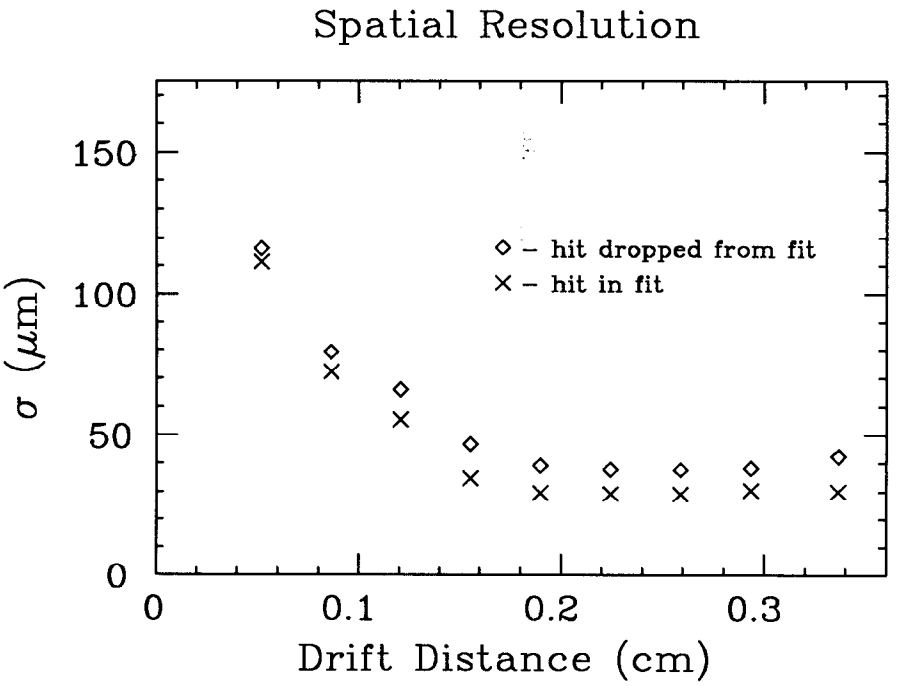


*Figure 19* VC Spatial Resolution. The fitted $\sigma$ of the residual distribution is shown as a function of drift distance. Both cases of hit left in the track fit and removed are shown. The true $\sigma$ is approximately half way between these two extremes.

hits were removed from the fit. The non-gaussian tails arise from the variation of resolution with drift distance. The resolution as a function of drift distance is shown in Figure 19. $\sigma$ as a function of drift distance both for the hit left in the fit, and removed. For most drift distances, the resolution is 35 $\mu$m. Near the wire the resolution degrades, most probably due to the dispersion in pulse heights in our gas mixture, which is underquenched. Estimates of degradation due to spacing of ionization clusters, and due to timing resolution, indicate that these do not provide the degradation of resolution near the wire. The mean resolution is 45 $\mu$m.

The figure of merit for lifetime measurements is $\sigma_v$, the resolution in extrapolated distance of closest approach to the geometric center of the chamber. $\sigma_v$ depends on the position resolutions of both the VC and the CD, the radii of their sense wires, and the amount of matter that causes multiple scattering in the beam pipe:

$$\sigma_v^2 \approx \frac{\overline{\sigma}^2}{N}(1. + f_1^2(\overline{\rho}) + f_2^2(\overline{\rho})) + \frac{\sigma_p^2}{p^2} \qquad [3.2]$$

The first term arises from the non-zero measurement resolution in the drift chambers, the second from multiple coulomb scattering. Here $f_1(x)$ and $f_2(x)$ represent the errors in extrapolation due to the slope and curvature in the fit, and are polynomials of order 1 and 2 respectively:

$$f_1(x) = x$$

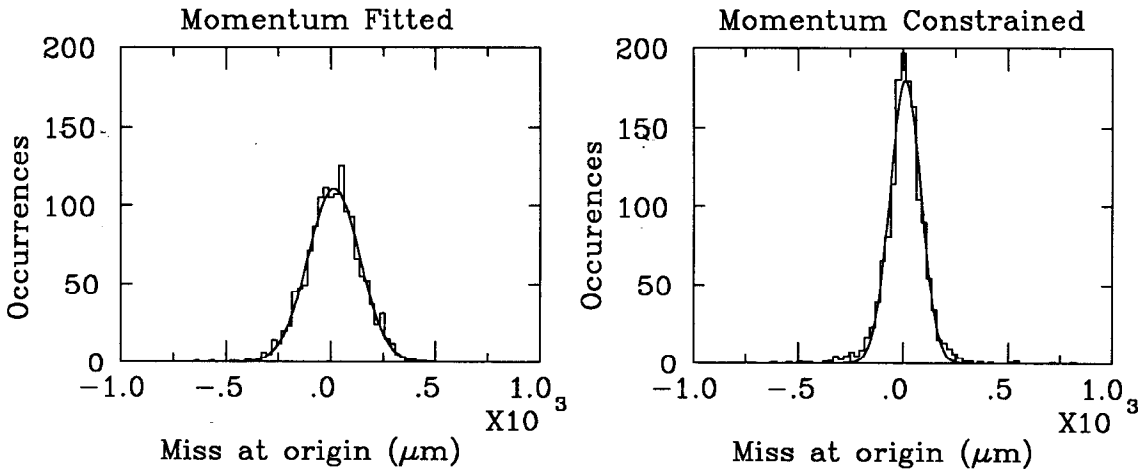


*Figure 20* 'Miss' distance in Bhabha Scattering Events. These data show the sum of the $\delta_0$s fort the two tracks in Bhabha events. On the left, the momenta were allowed to vary in the track fit. The distribution is very gaussian, with $\sigma = 124\,\mu$m. On the right, the track momenta were constrained to beam energy, and the distribution narrowed to $\sigma = 74\,\mu$m. This indicates the importance of the term arising from track *curvature* in [3.2].

$$f_2(x) = \frac{x^2 + \gamma_{1r}x + 1}{\gamma_{2r} + \gamma_{1r}^2 + 2}$$

$\overline{\rho}$, the dimensionless mean extrapolation distance, is $\overline{\rho} \equiv \overline{r}/\sigma_r$; given the radii $\{r_1, \ldots, r_N\}$ of the sensing layers, and their spatial resolutions $\{\sigma_1, \ldots, \sigma_N\}$,

$$\overline{r} \equiv \frac{\overline{\sigma}^2}{N}\sum_{i=1}^{N}\frac{r_i}{\sigma_i^2} \quad , \quad \frac{1}{\overline{\sigma}^2} \equiv \frac{1}{N}\sum_{i=1}^{N}\frac{1}{\sigma_i^2} \quad , \quad \sigma_r^2 \equiv \frac{\overline{\sigma}^2}{N}\sum_{i=1}^{N}\frac{1}{\sigma_i^2}(r_i - \overline{r})^2 \quad ,$$

and $\gamma_{1r}$ and $\gamma_{2r}$ are the coefficients of skew and curtosis defined in analogy with $\sigma_r$. For the combination of CD and VC, $\overline{r} = 8.6\,$cm, $\sigma_r = 7.4\,$cm, $\gamma_{1r} = 3.5$, and $\gamma_{2r} = 15$. $f_1^2(\overline{\rho}) = 1.4$, while $f_2^2(\overline{\rho}) = 12$, indicating that uncertainty in the curvature in the fit dominates the extrapolation error. This uncertainty arises primarily from the small maximum radius, 45 cm, of the MAC CD; the vertex resolution decreases as the *square* of this radius. The first term in [3.2] predicts a vertex resolution of $72\,\mu$m for $45\,\mu$m resolution in the VC. In the second term $\sigma_p$ depends on the angle of the track with respect to the beam axis, but was typically $65\,\mu$m- GeV/$c$.

The resolution in impact parameter was measured with Bhabha scattering events. Ideally, the opposing electron tracks would have equal and opposite impact parameters. Figure 20 shows the sum of the measured impact parameters. The distribution is very gaussian, with fitted $\sigma$ of $124\mu$m. This indicates a resolution $\sigma_v = 124/\sqrt{2} = 87\,\mu$m in impact parameter. Constraint of the momentum leads to $\sigma_v = 52\,\mu$m.

The effective spatial resolution in the VC degraded to $\approx 70\,\mu$m in multihadron events. The primary source of this degradation was the misassociation of hits

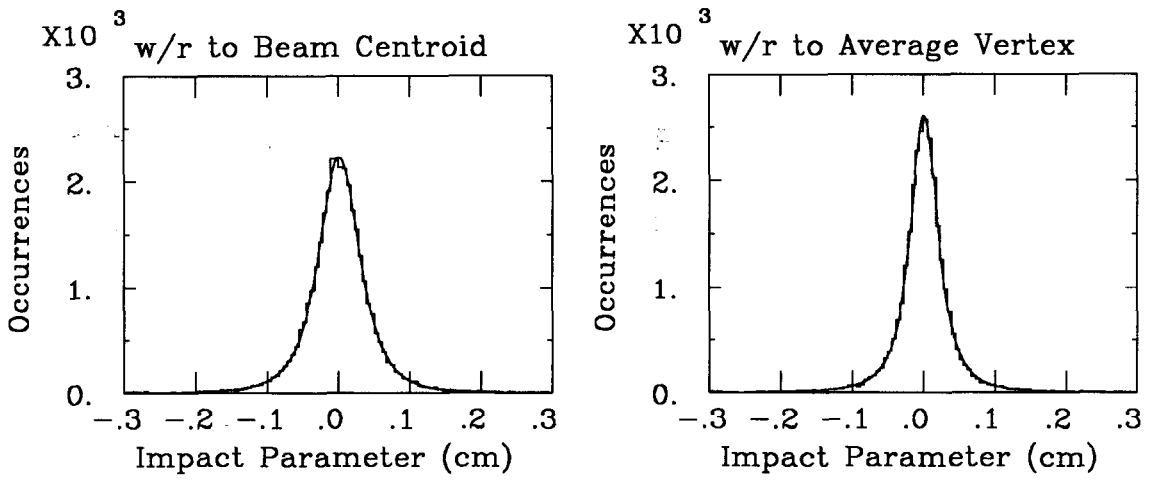


*Figure 21* Vertex Resolution in Multihadron Events. These data show the distance of closest approach of tracks with respect to two estimates of the $e^+e^-$ annihilation point. In the plot on the left, the estimate is the beam centroid, as determined in Bhabha scattering events. The fit is to a Student's $t$ distribution, with $\sigma = 306\,\mu$m and asymptotic power 1.9 describing the tails. In the plot on the right, the 'average vertex' was used; the fit yields $\sigma = 210\,\mu$m and power 1.5.

with tracks in the dense environment of a multihadron event. Hits in adjacent cells due to knock-on electrons probably caused some confusion as well.

The resolution in extrapolated distance of closest approach, or impact parameter, in multihadron events is given in Figure 21. Tracks with: 1) 3 or more hits in the VC; 2)7 or more hits in the CD; and 3) momenta $> 500\,$MeV/$c$ were used. The first plot makes use of the beam centroid, as determined from Bhabha scattering events on a run-by-run basis. The resolution in this case is dominated by the size of the beam itself, which we measured to have $\sigma_x = 350\,\mu$m and $\sigma_y = 70\,\mu$m. For the second plot, an improved estimate of the $e^+e^-$ annihilation location, the 'average vertex,' was made on an event by event basis. These data indicate a vertex resolution of $210\,\mu$m, of which $110\,\mu$m was due to multiple coulomb scattering.

Figure 22 exhibits the tracks and VC hits in a typical multihadron event. This event is in no way unusual in complexity or lack of noise.

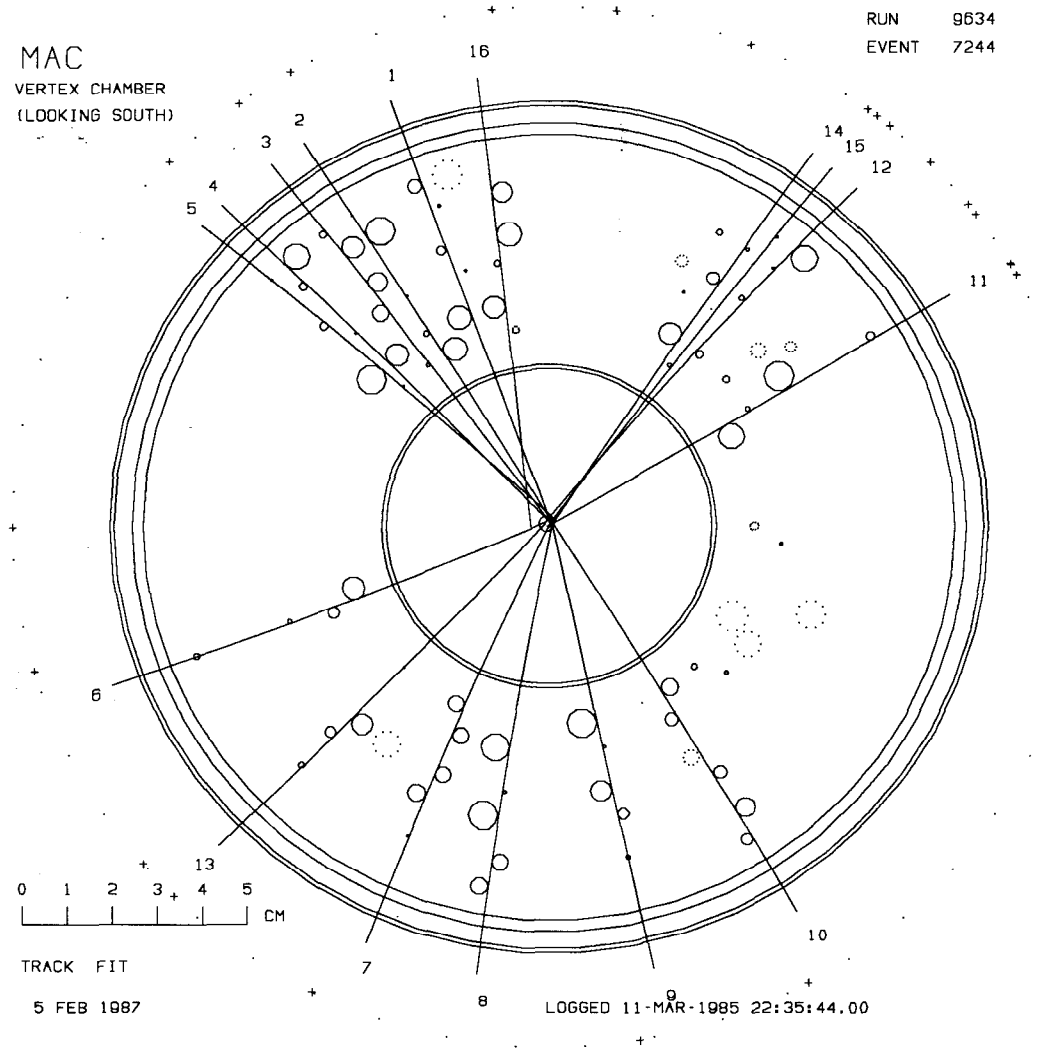


*Figure 22* A Typical Multihadron Event in the VC. Each small circle is the contour of constant drift distance found from the drift time measured in that cell. Solid circles indicate the hit was linked to a track; dotted indicate it was not. Tracks should be tangent to the small circles. The innermost small circles represent the beam pipe, the outermost the outer chamber wall and inner wall of the CD.

## $B$-Lifetime Measurement

Event selection We collected 94 pb$^{-1}$ of integrated luminosity, all at $\sqrt{s} = 29$ GeV, with the vertex chamber in place. This provided a sample of 44,000 multihadron events. We enrich a multihadron subsample in events from $b\bar{b}$ production by requiring a lepton with $p > 2$ GeV and $p_\perp > 1.5$ GeV, where $p_\perp$ was taken with respect to the calorimetric thrust axis.[16] The thrust axis is required to be $> 30°$ from the beam direction, and the thrust is required to exceed 0.72 to ensure that the axis is well measured.

A detailed description of the MAC detector can be found elsewhere.[13,15] Substantial improvements in the MAC muon identification have been made. MAC features an excellent system of external drift chambers to measure the exit direction of muons from the calorimeters. The steel in the hadronic calorimeters is toroidally magnetized, yielding a muon momentum measurement in addition to that provided by the central tracking inside our solenoid. We used the redundancy of the MAC systems to understand and improve our efficiencies and misidentification probabilities. The resulting $b\bar{b}$-enriched subsample tagged with muons contains 117 events for data taken with the VC. We have also reanalyzed the 101,000 multihadron events from $220\,\mathrm{pb}^{-1}$ of integrated luminosity accumulated prior to installation of the VC, and find 336 muon-tagged events.

We perform electron identification with the central electromagnetic calorimeter of MAC, and find 35 electron-tagged events in the data taken with the VC, and 74 in the data taken prior to VC installation. The electron sample is smaller than the muon sample due to smaller acceptance, and due to lower efficiency within that acceptance. A cut to reduce background from $2\gamma$ processes has been introduced that was not present in MAC's earlier $B$-lifetime analyses.

We estimate from Monte-Carlo and detector simulation studies that the events in the lepton tagged sample are 60% from $b\bar{b}$-production, 22% from $c\bar{c}$-production, and 18% from light quark production.

Lifetime Measurement

We use all tracks of sufficient measurement quality to estimate the $B$-hadron lifetime; previously, only the lepton tracks were employed. The quality cuts are: 1)$p > 0.5\,\mathrm{GeV}$; 2)number of CD hits $\geq 7$; and 3)number of VC hits $\geq 6$, in data where the VC was present. In the data with the VC, 4.4 tracks/event pass these criteria; in previous data, 6.3 tracks/event pass.

The *signed* impact parameter of tracks with respect to a point that estimates the $b\bar{b}$ production location is used to measure lifetime. The situation is exhibited in Figure 24. Since the signature of a non-zero lifetime is an average *positive* impact parameter, the sign convention is crucial. We use the calorimetric thrust axis to estimate the line of travel of the decaying parent; we assign an impact parameter a positive sign if it appears that the parent flew along the thrust axis into the hemisphere containing the track. This sign is uncorrelated with the sign conventions a host of systematic errors would provide.

Previously, we used the beam centroid, as determined from Bhabha scattering events, as our estimate of the $b\bar{b}$ production location. However, after addition of the VC, our resolution at the vertex is smaller than the beam, which we measure to have a half-width of $350\,\mu\mathrm{m}$ in the horizontal and $70\,\mu\mathrm{m}$ in the vertical. So, we have devised a method to improve our estimate of the $b\bar{b}$ production location on an event-by-event basis. Within each lepton-tagged event, we separate the $N$ tracks that pass the quality cuts into $N-1$ tracks which we then use to make a better estimate of the $b\bar{b}$ production location, and a track for which we measure the impact parameter. The improved estimate of the $b\bar{b}$ production location, or average vertex, is that point which maximizes a likelihood function constructed to represent the assumption that the $N-1$ tracks came from a common point, and that point came from the beam. We assume the log-likelihood is parabolic, and take the weights from the covariance matrix of the track fits, and the horizontal

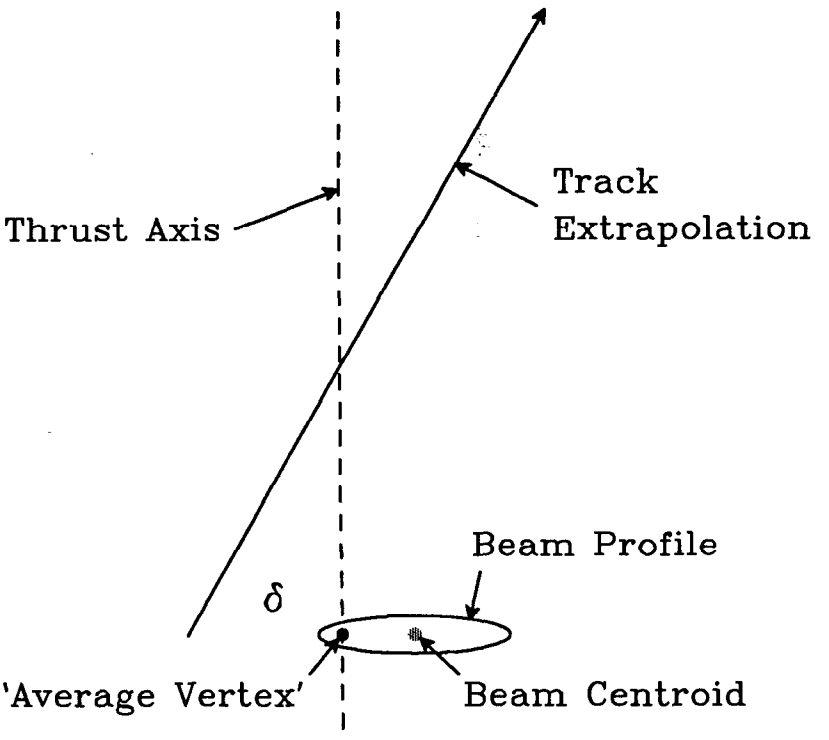


*Figure 24* Impact Parameter and Sign Definitions. We use the thrust axis to estimate the parent direction; if it appears that the parent flew forward along the thrust axis, then decayed, we assign $\delta > 0$. This diagram is a projection in the plane perpendicular to the beam; if the thrust axis and track have no components along the beam direction, $\delta > 0$ in this diagram. Negative impact parameters result most often from extrapolation error, but can result from backward decays.

and vertical beam size. We omit the track providing an impact parameter to avoid statistical correlations; we then loop over all quality tracks in the event, in turn omitting and defining a new average vertex for each track. The improvement yielded by the average vertex procedure was shown in Figure 23; the vertex resolution improves by some 50% compared to use of the beam centroid.

Tracks that are near the thrust axis in azimuth provide little information on non-zero parent flight paths, and are subject to sign errors induced by the error in thrust axis direction. Therefore, we cut tracks closer than $0.2/|sin(\theta_t)|$ radians in azimuth to the thrust axis, where $\theta_t$ is the polar angle of the thrust axis with respect to the beam axis. This leaves 2.9 tracks/event in the data taken with the VC, or a total of 441 tracks; 3.8 tracks/event, or 1558 tracks remain in the data set without the VC. The impact parameter distributions of these data are given in Figure 25.

We use the trimmed mean of the impact-parameter distribution as a robust estimator of the lifetime.[17] The trimmed mean is defined as the mean of a distribution where fractions $f$, in the tails, have been *symmetrically* removed. This estimator is robust in the sense that tails of the resolution function do not compromise the statistical precision of the estimator *and* in the sense that the

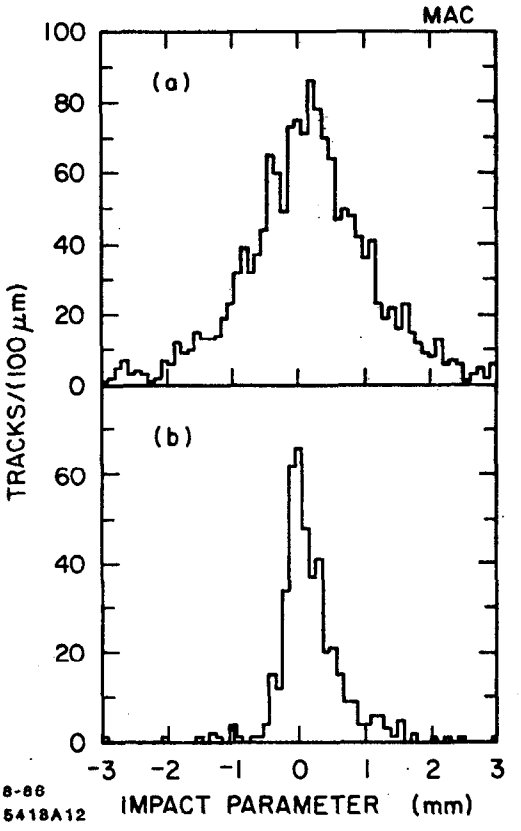


*Figure 25* Signed Impact Parameter Distributions. (a) 1558 tracks in lepton tagged events fromt the $220\,\mathrm{pb}^{-1}$ taken prior to installation of the VC. (b) 441 tracks in lepton tagged events taken in the $94\,\mathrm{pb}^{-1}$ accumulated with the VC. Not just the lepton tracks, but all tracks passing criteria described in the text are included. Both distributions show clear offsets from 0, and the VC data show an exponential-like tail.

trimmed mean, for a given lifetime, is insensitive to the shape of the distribution function. The statistical efficiency of the trimmed mean is be very near to that provided by a maximum likelihood fit, but the systematic error do to ignorance of the resolution function is substantially less than for a maximum likelihood fit. We find good statistical efficiency for $f = 0.1$, although the efficiency is insensitive to $f$ between 0.05 and 0.25. For the data taken with the VC, we find a trimmed mean of $129 \pm 19\,\mu$m, and $154 \pm 26\,\mu$m for previous data. The fraction $f$ was 0.1 in both cases.

We determine lifetimes using our Monte Carlo event generator and detector simulation. Because $b\bar{b}$ events have higher multiplicity than light quark events, the *track* fractions differ from the *event* fractions: we find that 70% of the tracks come from $b\bar{b}$ production; 16% from $c\bar{c}$ production, and 14% from light quark production.

The $B$ lifetime determined from the data taken with the VC is $\tau_b = 1.35 \pm 0.30(stat)$ps. Data taken prior to VC installation gives $\tau_b = 1.24 \pm 0.29(stat)$ ps. All electron tagged data yield $\tau_b = 0.92 \pm 0.35(stat)$ps, while all muon tagged

yield $\tau_b = 1.30 \pm 0.25(stat)$ ps. The combined result is $\tau_b = 1.29 \pm 0.20(stat)$ ps.

The dominant systematic error arises from uncertainty in how many tracks are produced in the primary hadronization of the $b$-quark; this arises primarily from the uncertainty in the mean fraction of the beam energy retained by the $B$-hadron. Taking this fraction to be $0.78 \pm 0.05$[18] indicates a $\pm 10\%$ uncertainty in the lifetime. This uncertainty is dominantly *multiplicative*, it does not degrade the *statistical* significance of the result. Other systematic uncertainties are discussed in (19). Our final combined result is $\tau_b = [1.29 \pm 0.20(\text{stat.}) \pm 0.07(\text{syst.})\,\text{ps}] \times (1.00 \pm 0.15)$, where the last factor is the systematic multiplicative uncertainty. This value is in agreement with the world average from PEP and PETRA detectors, $\tau_b = 1.26 \pm 0.16$ ps, where statistical and systematic errors have been combined in quadrature.

## CONCLUSIONS

The MAC vertex chamber, built of aluminized mylar proportional tubes, or straws, has achieved a spatial resolution of 35 $\mu$m, operated reliably in a region very close to colliding beams, and provided good data used to measure the $B$-hadron lifetime. The motivations and design considerations for this chamber have been reviewed, as has its performance and use for physics results. The attributes of this type of chamber make it an attractive option for use in high energy hadron colliders, such as the ELOISATRON.


## ACKNOWLEDGEMENTS

I wish to specially thank F. Villa, G. Charpak, and A. Zichichi for organizing this interesting and informative workshop, and the Ettore Majorana Center for wonderful hospitality. I wish to thank E. Askeland, J. Broeder, N. Erickson, J. Escalera, N. Palmer, the late C. T. Pulliam, J. Schroeder and D. Wright for their contributions to the vertex chamber design and construction.


## APPENDIX: TRACKING PARAMETERIZATION

Five parameters describe the helical trajectory of charged particles in the axial magnetic field of MAC. Three of these describe the circular projection of the trajectory in the plane perpendicular to the beam axis: $\kappa$, the reciprocal of the radius of curvature; $\delta_0$ the (signed) distance of closest approach of the circle to the geometric center of the MAC coordinate system; and $\phi_0$, the azimuth of the trajectory at closest approach. The sign of $\delta_0$ is determined from the cross product of the direction of the particle trajectory at closest approach taken with the direction from the geometric center to the point of closest approach. Figure 26 exhibits the the definition of $\kappa$, $\delta_0$, and $\phi_0$. The remaining two parameters describe the particle trajectory out of the plane perpendicular to the beam. $\theta$ is the angle with respect to the beam axis of the trajectory, and $z_0$ its intercept with the axis, viewed along the azimuth containing the distance of closest approach.

In the MAC track fitting routines, multiple coulomb scattering is described by 'kinks' at the radii of matter concentrations, such as the boundary between the VC and CD. Several kink angles are fit, but with a constraint by the r.m.s.

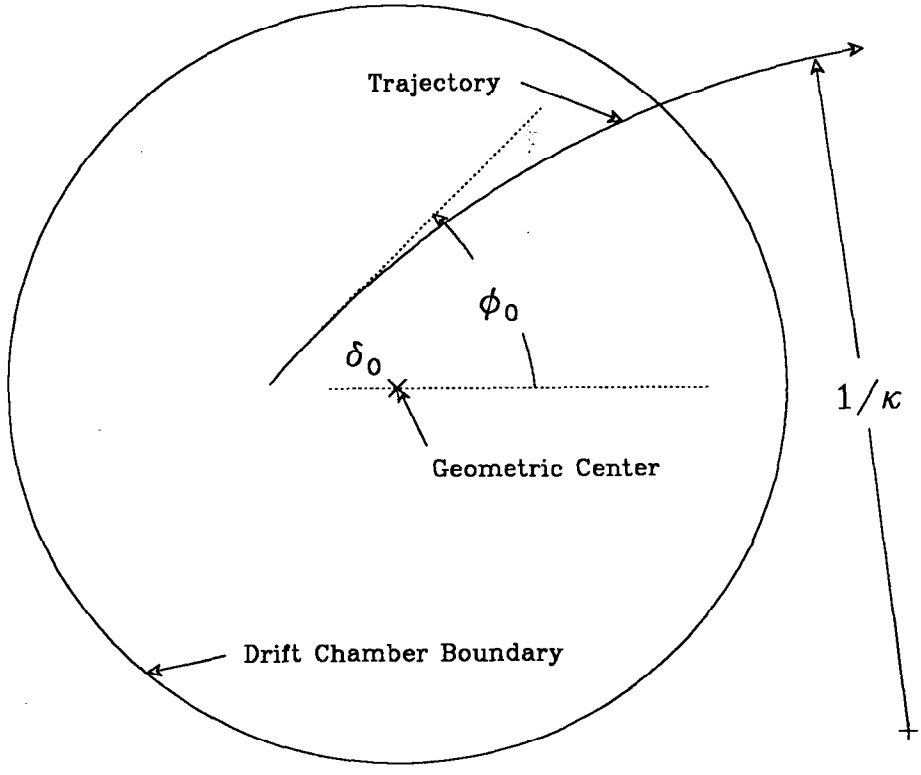


*Figure 26* Parameters Describing a Particle Trajectory. The figure is in the plane perpendicular to the beam. The outer circle schematically represents a boundary in the drift chamber system. $\delta_0$ is given a sign based upon the cross product of a vector pointing along the particle trajectory taken with a vector from the geometric center to the perihelion of the trajectory.

angle predicted by multiple coulomb scattering. This procedure quite naturally incorporates errors from multiple coulomb scattering into the covariance matrix of $\kappa, \delta_0, \phi_0, \theta$, and $z_0$.

## REFERENCES

1) The MAC collaboration consists of: W. W. Ash, H. R. Band, T. Camporesi, G. B. Chadwick, M. C. Delfino, R. De Sangro, W. T. Ford, M. W. Gettner, G. P. Goderre, D. E. Groom, R. B. Hurst, J. R. Johnson, K. H. Lau, T. L. Lavine, R. E. Leedy, T. Maruyama, R. L. Messner, J. H. Moromisato, L. J. Moss, F. Muller, H. N. Nelson, I. Peruzzi, M. Piccolo, R. Prepost, J. Pyrlik, N. Qi, A. L. Read, Jr., D. M. Ritson, F. Ronga, L. J. Rosenberg, W. D. Shambroom, J. C. Sleeman, J. G. Smith, J. P. Venuti, P. G. Verdini, E. von Goeler, H. B. Wald, R. Weinstein, D. E. Wiser, and R. W. Zdarko, *University of Colorado, INFN-Laboratori Nazionali di Frascati, University of Houston, Northeastern University, Stanford Linear Accelerator Center, Stanford University, University of Utah, and University of Wisconsin.*

2) E. Fernandez *et al.*, Phys. Rev. Lett. **51**, 1022 (1983); N. S. Lockyer

*et al.*, Phys. Rev. Lett. **51**, 1316 (1983).
3) M. Kobayashi and K. Maskawa, Prog. Theor. Phys. **49**, 652 (1973); P. H. Ginsparg, S. L. Glashow, and M. B. Wise, Phys. Rev. Lett. , **50**, 1415, (1983) and **51**, 1395, (1983).
4) D. Rust in *Proceedings of the Third International Conference on Instrumentation for Colliding Beam Physics, Novosibirsk, 1984*, (USSR Academy of Sciences, Siberian Division, Institute of Nuclear Physics, Novosibirsk, 1984); P. Baringer, C.K. Jung, H.O. Ogren, D.R. Rust, Nucl. Instrum. Meth. **A254**, 542 (1987).
5) G. Battistoni *et al.*, Nucl. Instrum. Meth. **A235**, 91 (1985).
6) E. Fernandez *et al.*, SLAC-PUB-3390, Aug. 1984, in *Proceedings of the Twelfth SLAC Summer Institute on Particle Physics, Stanford, 1984* edited by P.M. McDonough (Stanford Linear Accelerator Center, Stanford, 1984); W. Ash *et al.*, SLAC-PUB-4311, Apr. 1987, submitted to Nucl. Instrum. Meth.
7) G. Chadwick and F. Muller, MAC Internal Memo No. 683: this study employed the model described in J. Va'Vra, Nucl. Instrum. Meth. **225**, 445 (1984).
8) M. Breidenbach, F. Sauli, and R. Tirler, Nucl. Instrum. Meth. **108**, 23 (1973).
9) G.L. Godfrey "Proportional Tube Lifetimes (Magic Gas, A-$CO_2$, DME)," in *Workshop on Radiation Damage in Wire Chambers, Berkeley, CA*, edited by J. Kadyk (Lawrence Berkeley Laboratory, Berkeley, CA, 1986).
10) H.N. Nelson "Lifetime Tests for MAC Vertex Chamber," SLAC-PUB-4017, Jul. 1986, in *Workshop on Radiation Damage in Wire Chambers, Berkeley, CA*, edited by J. Kadyk (Lawrence Berkeley Laboratory, Berkeley, CA, 1986).
11) W.T. Ford *et al.*, Phys. Rev. **D33**, 3472 (1986).
12) D.E. Groom, Nucl. Instrum. Meth. **219**, 141 (1984).
13) E. Fernandez *et al.*, SLAC-PUB-4048 (in preparation), and to be published.
14) F. Solmitz, Ann. Rev. Nucl. Sci. **14**, 375 (1964).
15) E. Fernandez *et al.*, Phys. Rev. D **31**, 1066 (1985).
16) E. Fernandez *et al.*, Phys. Rev. Lett. **50**, 2054 (1983).
17) W. T. Eadie *et al.*, *Statistical Methods in Experimental Physics*, American Elsevier (1971).
18) This value and error result from our own analysis of world data. See E. H. Thorndike, Ann. Rev. Nucl. Sci. **35**, 195 (1985); S. Bethke, Z. Phys. C **29**, 175 (1985).
19) W.W. Ash *et al.*, Phys. Rev. Lett. **58**, 640 (1987).